

18 ABSTRACT:

19 The distinctive properties of single-walled carbon nanotubes (SWCNTs) have inspired the
20 development of novel applications in the field of cell nanobiotechnology. However, studies thus
21 far have yet to explore the effect of SWCNT functionalization on transport across the cell walls of
22 prokaryotes. We explore the uptake of SWCNTs in Gram-negative cyanobacteria and demonstrate
23 length-dependent and selective internalization of SWCNTs decorated with positively charged
24 proteins. The engineered SWCNTs enable protein delivery across the cell walls of both
25 filamentous and unicellular strains of cyanobacteria, independent of the strain's natural
26 competence for biomolecule delivery, with adsorption and internalization rate constants of $k_{\text{ads}} =$
27 $(9.08 \pm 0.16) \times 10^{-8} \text{ s}^{-1}$ and $k_{\text{in}} = (1.466 \pm 0.011) \times 10^{-4} \text{ s}^{-1}$, respectively. A custom-built, spinning
28 disc confocal microscope was used to image near-infrared (NIR) SWCNT fluorescence within
29 cells, revealing a highly inhomogeneous distribution of SWCNTs, and real-time monitoring of cell
30 division shows that the indefinitely photostable NIR fluorescence is inherited by daughter cells.
31 The augmented cells maintain sustained photosynthetic activity and growth, as well as a seven-
32 fold enhancement in photo-exoelectrogenicity, and we exploit these nanobionic characteristics in
33 continuous imaging and biophotovoltaic applications.

34

35

36

37 **1. Introduction**

38 The internalization of carbon nanotubes in living cells forms the basis for new technologies in
39 cellular imaging, gene and drug delivery, and other biological and medical whole-cell
40 applications^{1,2}. Numerous synthetic and biological molecules can be immobilized on the surface
41 of carbon nanotubes which, when appropriately functionalized, are capable of crossing biological
42 barriers and binding specific molecular targets. Single-walled carbon nanotubes (SWCNTs) in
43 particular have optoelectronic properties that are well suited for phototherapy³, imaging⁴, and
44 sensing⁵⁻⁸. Unlike conventional fluorescent probes, the electronic bandgap of semiconducting
45 SWCNTs allows these nanostructures to absorb light across a wide range of the electromagnetic
46 spectrum and to re-emit the absorbed energy as near-infrared (NIR) fluorescence. This
47 fluorescence remains photostable even upon continuous exposure to high-intensity
48 illumination^{9,10}. SWCNT fluorescence can optically penetrate biological tissue and biofluids for
49 deep-tissue imaging. Furthermore, the fluorescence provides an optical signal that is distinct from
50 the autofluorescence of biological fluorophores that emit in the visible range. SWCNTs have been
51 used for subcellular targeting to the cell nucleus and peri-nuclear regions^{11,12}, and their
52 semiconducting properties have been exploited for the phototherapeutic treatment of cancer cells³.
53 Recently, semiconducting SWCNTs have been shown to enhance the photosynthetic efficiency of
54 light-harvesting organelles extracted from plant cells¹³ and enable nitroaromatic detection in living
55 spinach leaves¹⁴.

56 The majority of studies to date have focused on interfacing SWCNTs with cells of eukaryotic
57 organisms, for which both active and passive uptake mechanisms of SWCNTs have been
58 reported¹⁵⁻¹⁸. Previous studies have shown that SWCNT surface modifications are critical to either
59 promote or hinder nanoparticle penetration through the cell membrane of eukaryotes^{13,15}. By

60 contrast, no work has so far explored the influence of functionalization on SWCNT transport
61 across the complex, multilayered walls that surround bacterial cells. While the interaction of
62 modified nanotubes with *Escherichia coli* cells has been studied¹⁹, bacterial uptake of fluorescent
63 SWCNTs has yet to be reported. A comprehensive study focusing on the physiochemical factors
64 that affect SWCNT transport across the cell wall architecture of prokaryotes, which is currently
65 lacking in the field, is the first step in enabling engineered bacterial nanoprobes for targeted and
66 controlled biomolecule delivery. Beyond delivery, the SWCNT fluorescence allows for
67 spatiotemporal intracellular sensing^{20,21}, NIR cell imaging²², and augmented light-harvesting
68 applications¹³ in phototrophic strains.

69 These applications motivate the current study, which focuses on tuning non-covalent surface
70 functionalization to facilitate the uptake of fluorescent SWCNTs in bacterial cells. We focus our
71 investigation on phototrophic cyanobacteria, selected for several reasons. First, cyanobacteria
72 possess a complex cell wall structure that forms a considerable permeability barrier. Like other
73 bacteria, cyanobacteria are surrounded by a rigid peptidoglycan (PGN) cell wall that determines
74 the characteristic cell shape, while protecting it against mechanical stress and rupture. The PGN
75 layer is enclosed by an outer membrane, which is typical of Gram-negative cells. However,
76 compared to other Gram-negative bacteria, the PGN wall found in cyanobacteria is considerably
77 thicker (about 10 nm in unicellular strains) and shows a higher degree of cross-linkage, similar to
78 Gram-positive bacteria²³. Also, the presence of a crystalline surface layer (S-layer) in some species
79 can further limit the translocation of proteins and other high-molecular-weight substances across
80 the outer membrane²⁴. Since the transformation of cyanobacteria with foreign DNA often relies on
81 bacterial conjugation based on multiple plasmids and triparental mating strategies, the ability to
82 genetically manipulate these microorganisms can also be limited²⁵. SWCNT translocation across

83 cyanobacterial cell walls could therefore facilitate the delivery of larger synthetic or bio-molecules,
84 including genetic material and proteins, as previously demonstrated for eukaryotic cells²⁶⁻²⁸.
85 In addition to the considerable permeability barrier, cyanobacteria are photosynthetic cells that
86 demonstrate optical properties complementary to those of semiconducting SWCNTs. Owing to
87 their excellent conductivity and elevated electroactive surface area, SWCNTs have been shown to
88 enhance the efficiency of the light reactions of photosynthesis both *in vivo* and *in vitro*¹³,
89 motivating several optical, energy-based applications. Although the photosynthetic effects of
90 SWCNTs have yet to be studied in microbes, electrodes based on conductive multi-walled carbon
91 nanotubes, have been shown to boost microbial device efficiencies through more efficient charge
92 extraction.²⁹ Furthermore, the photosynthetic pigments in cyanobacteria autofluoresce at
93 wavelengths overlapping with the fluorescence emissions of fluorophores emitting in the visible
94 region typically used for bioimaging and sensing. Therefore, the NIR emissions of SWCNTs
95 motivate their use in mitigating this spectral overlap for fluorescence imaging and tracking. In the
96 present study, we demonstrate the applicability of internalized SWCNTs as NIR imaging probes
97 for the model cyanobacterium *Synechocystis* sp. PCC 6803 (hereafter *Synechocystis*), using a
98 combination NIR and visible imaging, Raman spectroscopy, and immunogold labeling
99 transmission electron microscopy (TEM). We further characterize the viability of cells
100 incorporating these nanoprobe and show enhanced photocurrent generation when these
101 nanobionic cells are incorporated into an electro-chemical device.

102 **2. Results and Discussion**

103 SWCNTs were non-covalently functionalized with various coatings shown to preserve SWCNT
104 fluorescence and subsequently screened for their internalization efficiency. We compared uptake
105 by *Synechocystis* cells to uptake by isolated spinach chloroplasts, photosynthetic organelles

106 surrounded by a double membrane lacking a PGN layer. *Synechocystis* cells and chloroplasts were
107 immobilized onto poly-lysine coated glass-bottom dishes and exposed to a 2 mg/L aqueous
108 suspension of SWCNTs functionalized with DNA-, chitosan-, or lysozyme (LSZ) for 10 minutes.
109 After washing with HEPES buffer, the interaction of SWCNTs with the bacterial cells and
110 chloroplasts was probed using NIR fluorescence microscopy (**Figure 1a**). Chloroplasts incubated
111 with DNA- or chitosan-wrapped SWCNTs show co-localization of the SWCNT NIR-fluorescence
112 signal and autofluorescence of the chloroplasts' photosynthetic pigments. This observation is in
113 agreement with previous studies^{13,15} that have shown rapid localization of DNA- and chitosan-
114 wrapped SWCNTs within the organelle. By contrast, no NIR fluorescence signal was observed for
115 *Synechocystis* cells (**Figure 1b**), suggesting that the DNA- and chitosan-wrapped SWCNTs are
116 unable to penetrate the cell wall. Furthermore, varying SWCNT concentration or incubation time
117 did not result in detectable NIR-fluorescence from these conjugates inside or near the cells (data
118 not shown).

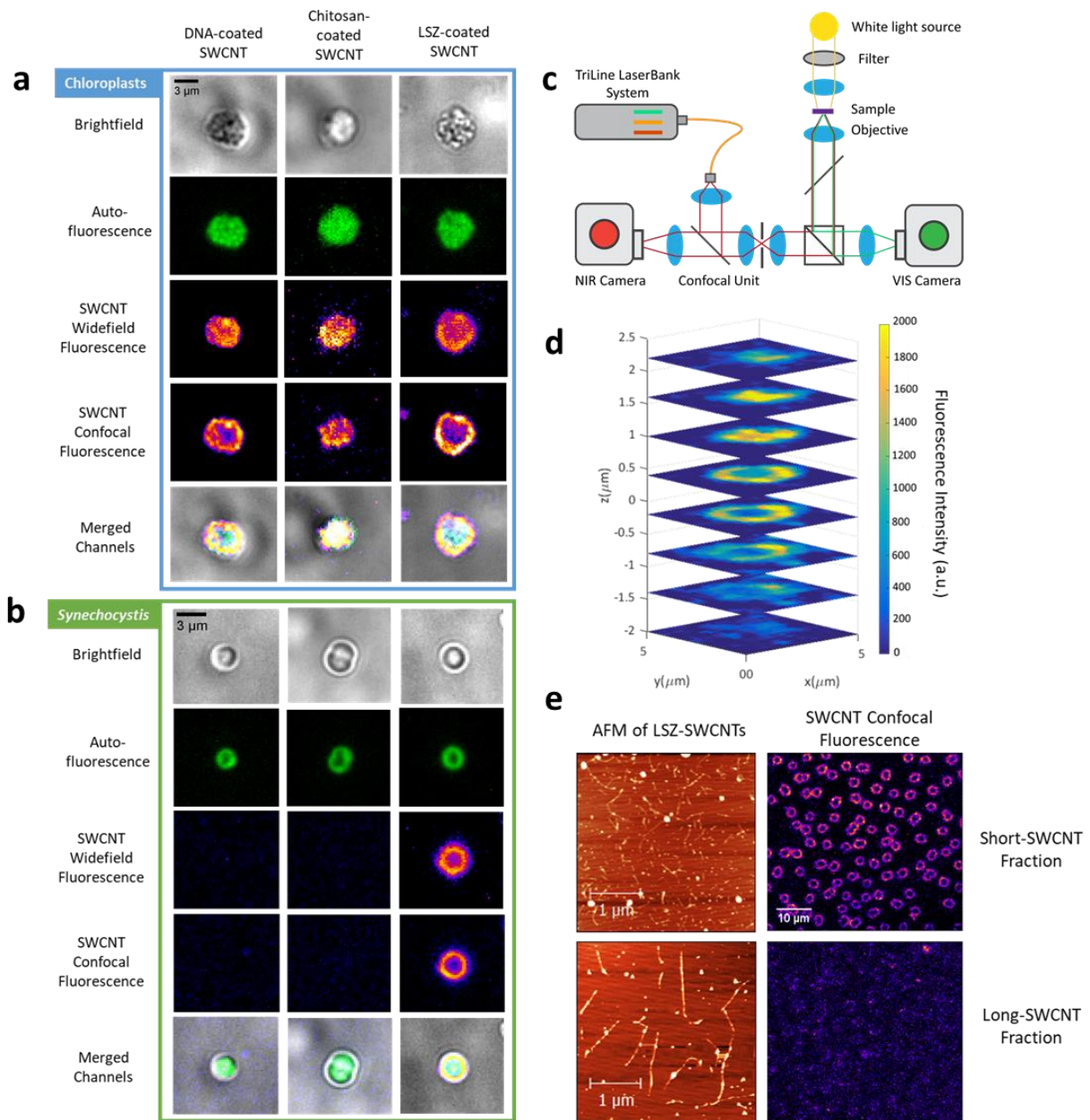
119 Unlike the DNA and chitosan, the LSZ-wrapped SWCNTs (LSZ-SWCNTs) show NIR
120 fluorescence that co-localizes with the autofluorescence of both the photosynthetic organelles and
121 *Synechocystis* cells. Containing only 129 residues, LSZ serves as a small model protein whose
122 folding kinetics and interaction with SWCNTs has been well-studied³¹⁻³³. This enzyme is known
123 to disrupt the PGN layer of bacteria through muramidase activity and has been shown to retain its
124 tertiary structure when immobilized on SWCNTs³⁴. The resulting nano-biohybrid complexes
125 retain enzymatic activity both in solution and in solid assemblies³⁴. As such, LSZ-SWCNTs have
126 been used to produce high strength, antimicrobial fibers and films³⁵⁻³⁷. The cellular uptake of LSZ-
127 SWCNTs has only been investigated in eukaryotes; while LSZ-stabilized gold nanoparticles were
128 internalized by mouse embryonic fibroblasts through receptor-mediated endocytosis³⁸,

129 internalization of LSZ-SWCNTs in the same cells was not observed³⁹. The lack of internalization
130 has been attributed to the poor stability of the LSZ-SWCNT dispersions in cell culture media.
131 Conversely, no measurable flocculation of LSZ-SWCNTs was observed in the 1 mM HEPES
132 buffer used in this study (**Figure S1**).

133 To establish the precise distribution of LSZ-SWCNTs within cells, we used a custom-built
134 confocal microscope for NIR detection. This unique setup, schematically represented in **Figure**
135 **1c**, consists of a customized spinning-disc unit with a NIR anti-reflection coating on the lenses,
136 enabling unrivaled real-time monitoring of SWCNT NIR fluorescence⁴⁰. In contrast to the
137 widefield NIR measurements, the increased spatial resolution of the confocal mode clearly
138 revealed a heterogeneous distribution of SWCNT fluorescence inside the cells (**Figure 1b and**
139 **1d**). The overlay of the confocal SWCNT fluorescence and bright-field images of *Synechocystis*
140 shows enhanced SWCNT fluorescence overlapping with the peripheral regions of the cells
141 (**Figures 1b and Figure S2**), an observation that is consistent with previous nanoparticle uptake
142 studies¹⁹. These findings suggest that the majority of the LSZ-SWCNTs lie within the periplasmic
143 region, with significantly less SWCNT fluorescence observed in the cytoplasmic space and in the
144 autofluorescent thylakoid membranes that accommodate the light-harvesting, photosynthetic
145 complexes.

146

147



148

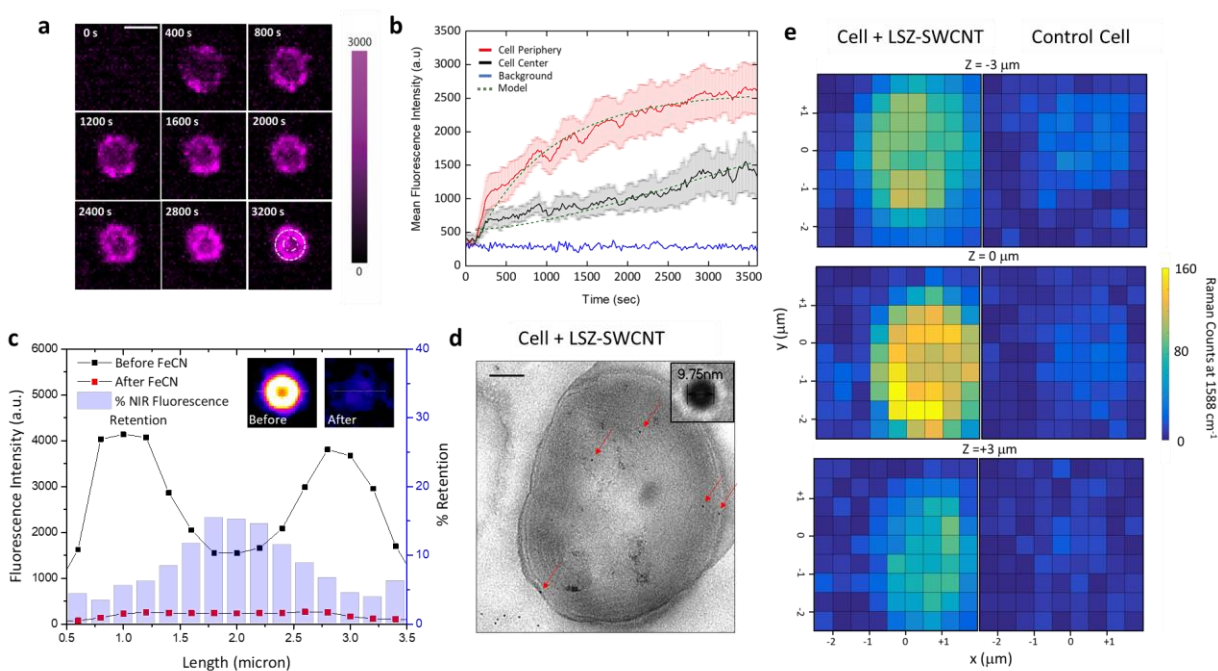
149 **Figure 1 | NIR Imaging of Internalized SWCNTs.** Representative images of (a) chloroplasts and (b) *Synechocystis*
 150 cells after incubation with DNA-, chitosan-, or LSZ-wrapped SWCNTs. Fluorescence intensity was recorded for cell
 151 autofluorescence (excitation at 640 nm, emission above 800 nm), SWCNTs in widefield mode (excitation at 780 nm,
 152 emission above 800 nm, at 1.8 mW/cm²), and SWCNTs in confocal mode (excitation at 780 nm, emission above 800
 153 nm, at 3.7 mW/cm²). (c) The custom-built, NIR confocal setup used to image internalized SWCNTs consists of a 500
 154 mW laser coupled to an inverted microscope body. The spinning-disc confocal head contains transmission lenses with
 155 an anti-reflective NIR coating. An indium gallium arsenide (InGaAs) camera is used for imaging. (d) Z-stacked

156 confocal images of *Synechocystis* show the SWCNT distribution throughout the cell. **(e)** AFM images of short and
157 long fractions of length-separated SWCNTs (top and bottom respectively). Confocal fluorescence images of wild-
158 type *Synechocystis* cells incubated with 2 mg/L of short (top) and long (bottom) LSZ-SWCNT fractions.

159
160 The contribution of length to the nanoparticle localization within *Synechocystis* cells was studied
161 using length-fractionated LSZ-SWCNTs. **Figure 1e** presents atomic force microscopy (AFM)
162 images of two fractions of length-separated SWCNTs, containing short (210 ± 83 nm) and long
163 (836 ± 362 nm) SWCNTs. A fluorescence comparison of the two fractions confirm that the longer
164 SWCNTs exhibit higher fluorescence intensity (at 780 nm excitation) than the shorter SWCNTs
165 at the same nanotube concentration (**Figure S3**), in agreement with previous reports⁴¹⁻⁴³. Despite
166 the lower quantum yield, cells incubated with the shorter LSZ-SWCNTs showed significantly
167 higher NIR fluorescence (**Figure 1e**) compared to those incubated with the longer LSZ-SWCNTs.
168 The elevated fluorescence levels suggest a preferential accumulation of short LSZ-SWCNTs inside
169 *Synechocystis*. These observations are in agreement with Boyer et al. and Kang et al.^{43,44}, who
170 reported a length dependence of nanoparticle uptake inside mammalian cells. Becker and co-
171 workers⁴⁵ have similarly observed that only DNA-wrapped SWCNTs shorter than 189 ± 17 nm
172 were able to access the internal cellular compartments, whereas longer SWCNTs remained in the
173 culture medium.

174 Although the nanobionic cells showed significant NIR fluorescence at the cell center, the enhanced
175 fluorescence signal in the cytoplasmic space could arguably originate from out-of-focus
176 periplasmic SWCNT fluorescence, rather than from SWCNTs that crossed the cytoplasmic
177 membrane into the central cell volume. To explore this possibility, we monitored the LSZ-SWCNT
178 interaction with *Synechocystis* cells in real-time during a 1 h incubation with a 2 mg/L LSZ-
179 SWCNT suspension. We separately analyzed SWCNT fluorescence intensity change either near

180 the cell envelope or in the inner compartments of the cell including the thylakoid membranes and
 181 cytosolic space (**Figure 2a**). Following the addition of the SWCNTs, we observe a rapid increase
 182 in fluorescence at 200 seconds along both the periphery and the central part of the cell (**Figure**
 183 **2b**). At the cell periphery, the sharp initial increase is followed by a more gradual increase of
 184 fluorescence that levels off during the course of the measurement. By contrast, although SWCNT
 185 fluorescence in the cell center increases slowly following the initial jump, the rate of this
 186 enhancement accelerates over time. This spatiotemporal difference in NIR localization suggests
 187 that the fluorescence signal at the cell center originates, at least partially, from SWCNTs slowly
 188 accumulating inside the cell, and it therefore cannot entirely be attributed to contaminating
 189 fluorescence from the substantially brighter cell periphery.
 190



191
 192 **Figure 2 | Localization of Internalized SWCNTs.** (a) Time-lapse NIR confocal images of SWCNT fluorescence
 193 inside the cell. The concentric dashed circles in the last frame indicate the cell periphery and center of the cell. Scale
 194 bar = 3 μm . (b) Corresponding mean fluorescence variations over time measured along the periphery (red) and center

195 (black) of *Synechocystis* cells compared to background (blue) during internalization. Quantitative measurements are
196 averaged among $n=12$ cells. The results of the fitted kinetic model at the periphery and at the center of the cell is
197 shown in green ($R^2 = 0.97$). (c) SWCNT fluorescence along the cell diameter traced from a representative
198 *Synechocystis* cell (inset) is reported before (black line) and after (red line) addition of 120 mM ferricyanide. The ratio
199 between the fluorescence intensities after and before the addition of ferricyanide is represented with a blue histogram,
200 as percentage of fluorescence retention inside the cell. (d) TEM sections of *Synechocystis* cells treated with 2 mg/L
201 LSZ-SWCNTs labeled with anti-lysozyme antibody and 10 nm gold-labeled secondary antibody. Gold nanoparticles
202 inside *Synechocystis* cells are indicated with red arrows. Scale bar = 500 nm. (e) Representative confocal 3D Raman
203 mapping of the characteristic SWCNT G'-band (at 1580 cm^{-1}) under 532 nm laser excitation, used to explore the
204 spatial distribution of LSZ-SWCNTs within *Synechocystis* cells. Scans were performed at different heights Z within
205 the cells, with $Z=0\text{ }\mu\text{m}$ corresponding to the focal plane of the cell exhibiting the highest image contrast in the bright-
206 field imaging mode. The images show the comparison of a LSZ-SWCNT-treated cell with a non-treated cell at
207 different heights along the z-axis. The Raman signal at 1580 cm^{-1} can be attributed to SWCNTs that accumulated
208 within the cell.

209

210 The penetration of SWCNTs into the cytoplasm was further studied by monitoring their
211 fluorescence response following the addition of ferricyanide. Ferricyanide is a redox active
212 molecule capable of SWCNT fluorescence quenching⁴⁶. Although this anionic compound is unable
213 to penetrate the plasma membranes of eukaryotes, studies have shown that it can access the
214 periplasmic space of intact cyanobacterial cells without penetrating their inner membrane^{47,48}. The
215 addition of ferricyanide (**Figure 2c**) resulted in significantly higher quenching of LSZ-SWCNT
216 fluorescence at the cell periphery compared to the cell center. Calculating the ratio of NIR
217 fluorescence pre- and post-addition (**Figure 2c**) showed that while only 3-5% of the initial
218 SWCNT fluorescence at the cell periphery was preserved, a significantly higher amount of 15%
219 was retained at the cell center. Furthermore, the addition of excess ferricyanide did not reduce
220 intracellular NIR fluorescence emissions to background levels (data not shown). Since

221 *Synechocystis* cells do not exhibit significant autofluorescence in absence of SWCNTs at the same
222 imaging conditions (**Figure S4b** and **Figure S5c**), these results further suggest that the retained
223 NIR signal at cell center originates from a fraction of SWCNTs reaching the inner compartments
224 of the cells.

225 As an additional method to validate the ability of LSZ-SWCNTs to access the inner compartments
226 of *Synechocystis*, we probed the presence of intracellular lysozyme proteins by immunogold
227 labeling and TEM. A representative image of a section of a *Synechocystis* cell treated with 2 mg/L
228 LSZ-SWCNTs confirmed the localization of the gold nanoparticles within the cell (**Figure 2d**).
229 The majority of gold nanoparticles were observed to preferentially localize within the cell wall
230 and over the thylakoid membranes of cells treated with LSZ-SWCNTs, whereas the cytoplasmic
231 space contained significantly fewer particles (**Figure S6**). In contrast to the cells incubated with
232 the labelled LSZ-SWCNTs, cells treated with excess LSZ showed no internalized gold
233 nanoparticles within the cells (**Figure S6**), indicating both an absence of unspecific labeling and
234 the inability of the protein alone to penetrate intact cells of *Synechocystis*. These findings are in
235 agreement with previous reports that have demonstrated the inefficacy of LSZ on *Synechocystis*
236 cells in the absence of additives such as EDTA, DTT, or spermine.^{49,50} This resistivity to lysis is
237 attributed to the protective S-layer surrounding the outer membrane as well as to the robust PGN
238 layers discussed above⁵¹. Additional control experiments, where the anti-LSZ antibody was
239 omitted, also lacked gold nanoparticles within the cell sections (**Figure S6**).

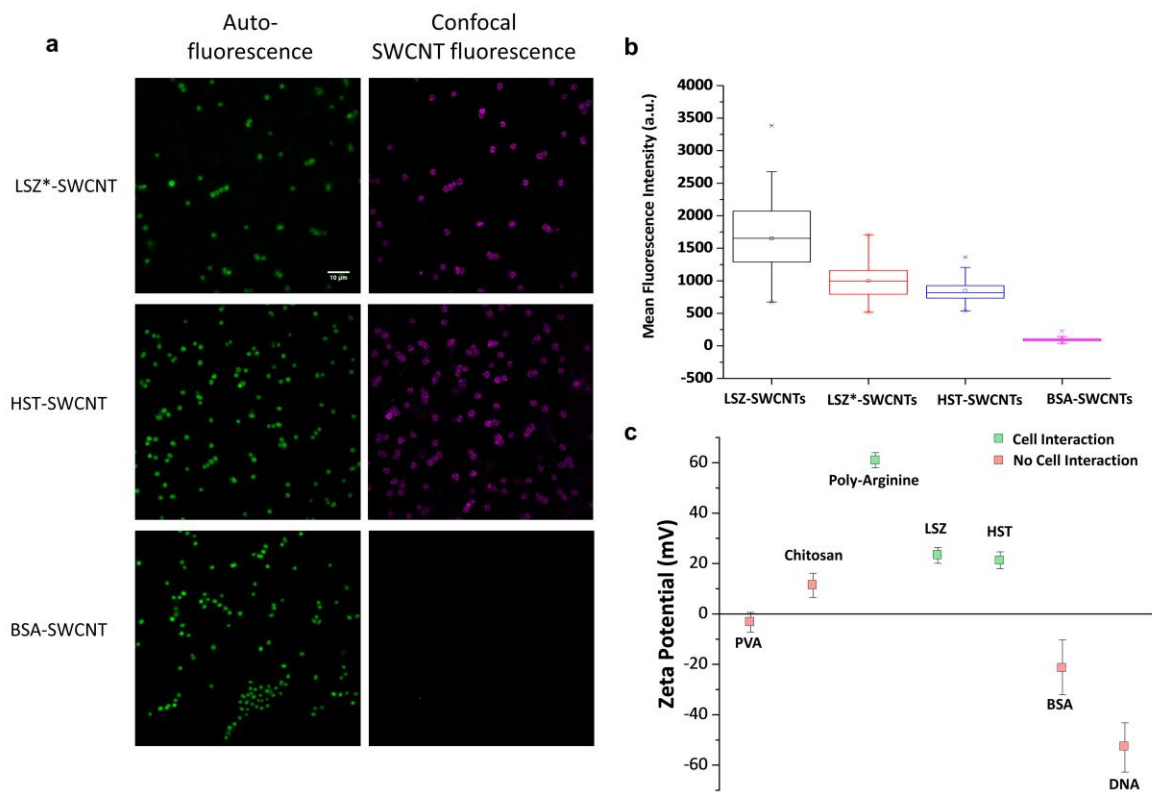
240 The intracellular distribution of LSZ-SWCNTs inside *Synechocystis* cells was further confirmed
241 using confocal Raman spectroscopy (**Figure 2e**). Confocal Z-scan maps of the characteristic G-
242 band at 1588 cm⁻¹ showed that the SWCNT signal was distributed throughout the volume of the
243 cell, with elevated intensity located at the cell periphery (**Figure 2b and S7a**), supporting our

244 observations from confocal fluorescence images. We further noted an increase in the D to G band
245 ratio of the nano-biohybrid particles upon internalization, in agreement with other cell studies⁵²,
246 suggesting possible modification of the LSZ-SWCNTs following internalization.

247 The underlying mechanism for LSZ-SWCNT internalization was studied by evaluating the
248 influence of the enzymatic muramidase activity on SWCNT uptake. *Synechocystis* cells were
249 incubated with SWCNTs functionalized with thermally inactivated LSZ (**Figure 3**), which is
250 unable to hydrolyze the PGN network³³. Interestingly, as shown in the top panel of **Figure 3a**, the
251 inactive LSZ-SWCNTs (LSZ*-SWCNTs) localized within *Synechocystis* cells to a similar extent
252 as LSZ-SWCNTs. This observation suggests that the inherent physiochemical protein
253 characteristics, such as charge, rather than enzymatic activity, are likely responsible for
254 nanoparticle internalization.

255 In agreement with this hypothesis, previous reports have shown that the hydrophobic and cationic
256 properties of inactive LSZ as well as engineered peptides can still interact with bacterial
257 membranes^{53 54}. This hypothesis was tested by comparing the localization of SWCNTs
258 functionalized with bovine serum albumin (BSA) and histone H1 from *bos taurus* (HST), which
259 demonstrate distinct physiochemical characteristics. BSA is a medium-sized protein ($MW_{BSA} =$
260 66.5 kDa) present in blood serum. This protein has been previously conjugated to SWCNTs for
261 intracellular nanoparticle delivery in eukaryotic cells²². On the other hand, HST is a small protein
262 ($MW_{HST} = 21.5$ kDa) that is structurally similar to LSZ. It contains a high content of basic residues,
263 which assist in cation- π interactions on the nanotube surface, and it possesses an overall positive
264 charge at physiological pH⁵⁵. NIR confocal images (**Figure 3a**) showed uptake of HST-SWCNTs
265 that was comparable to both LSZ-SWCNTs and LSZ*-SWCNTs. In contrast to HST-SWCNTs,
266 no NIR fluorescence was detected within cells incubated with BSA-SWCNTs. A quantitative

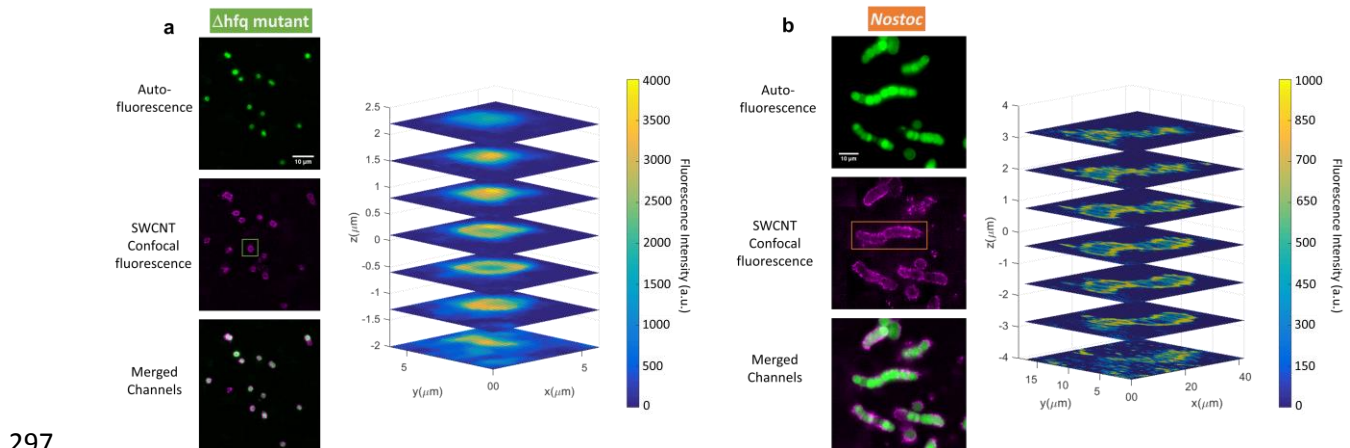
267 comparison of the mean NIR fluorescence intensities of LSZ-, LSZ*-, HST-, and BSA-SWCNTs
 268 in individual cells confirmed minimal uptake for BSA-SWCNTs (**Figure 3b**). Zeta-potential
 269 measurements of the functionalized SWCNTs (**Figure 3c**) revealed that wrappings that facilitate
 270 cellular uptake possess positive surface potentials above 20 mV at pH 7.4. Additional experiments
 271 with functionalized-SWCNTs possessing even higher zeta-potentials, such as poly-arginine
 272 SWCNTs (≈ 61 mV), confirmed this observation (**Figure S8**). These measurements suggest that
 273 the considerable positive surface charge of the protein corona drives the electrostatic interaction
 274 between the SWCNT conjugates and the negatively charged cell envelope, which in turn facilitates
 275 the penetration of the nanoparticles inside the cell. This mechanism is consistent with the results
 276 of Pedersen *et al.*, who have shown that positively charged nanoparticles are prone to interact with
 277 negatively-charged lipopolysaccharide-containing leaflets of Gram-negative bacterial cell walls⁵⁶.



279 **Figure 3 | Effect of Surface Charge on SWCNT Uptake. (a)** Comparison of widefield autofluorescence (excitation
 280 at 640 nm, emission above 800 nm) (left) and NIR confocal images (excitation at 780 nm, emission above 800 nm)
 281 (right) of *Synechocystis* cells incubated with LSZ⁻, HST⁻, and BSA- SWCNTs. **(b)** The corresponding mean NIR
 282 fluorescence intensity determined from n=51 (LSZ), n=37 (LSZ^{*}), n=67 (HST), and n=121 (BSA) individual cells.
 283 **(c)** Zeta-potential of SWCNTs functionalized with PVA, chitosan, poly-arginine, LSZ, HST, BSA and DNA in 1 mM
 284 HEPES buffer at pH 7.4. Nanoparticles that interact with *Synechocystis* cells are shown in green whereas those that
 285 do not are shown in red. Measurements were performed in triplicates.

286

287 While eukaryotic cells have shown nanoparticle permeation *via* energy-dependent endocytosis⁵⁷,
 288 no known active mechanisms exist for the uptake of supramolecular complexes, such as
 289 conjugated SWCNTs, in cyanobacteria. One means of uptake could occur *via* type IV pili (T4P),
 290 retractable appendages that are not only involved in cell motility, but are also crucial for the uptake
 291 of exogenous DNA in some bacteria, including *Synechocystis*⁵⁸. To evaluate if T4P facilitate
 292 SWCNT uptake, a mutant strain of *Synechocystis*, lacking T4P (Δhfq)⁵⁹ was incubated with LSZ-
 293 SWCNTs. Fluorescence images (**Figure 4a**) show that uptake by Δhfq cells was comparable to
 294 wild type *Synechocystis* cells, demonstrating that T4P are not required for internalization.
 295 Moreover, LSZ-SWCNT uptake was also observed in *Nostoc sp.* (hereafter *Nostoc*) (**Figure 4b**),
 296 a multicellular filamentous strain that does not assemble T4P in the vegetative state⁶⁰.



298 **Figure 4 | SWCNT Internalization by Strains Lacking Pili for DNA Uptake.** Representative images of
 299 cyanobacteria lacking natural competence, including (a) *Synechocystis Δhfq* and (b) *Nostoc* cells. Cells incubated with
 300 LSZ-SWCNT show cell autofluorescence (excitation at 640 nm, emission above 800 nm) (top), and confocal SWCNT
 301 fluorescence (excitation at 780 nm, emission above 800 nm) obtained after complete photobleaching of the cell
 302 (middle). An overlay of the fluorescence emissions is shown on the bottom, alongside stacked confocal images of the
 303 boxed cell in the axial direction.

304

305 The uniform uptake of SWCNTs by non-piliated cells suggests that uptake likely proceeds through
 306 a passive membrane penetration mechanism based on charge-dependent binding of SWCNTs to
 307 the negatively-charged cell wall prior to internalization. Based on this proposed mechanism,
 308 SWCNT uptake in cyanobacterial cells can be modeled as a two-step internalization mechanism:



310 where \mathbf{SWCNT}_{buffer} represents free SWCNTs in solution, \mathbf{SWCNT}_{bound} represents SWCNTs that
 311 have adsorbed to the cell wall, and \mathbf{SWCNT}_{in} represents SWCNTs that have been internalized by
 312 the cell. The adsorption and internalization rate constants are k_{ads} and k_{in} , respectively. In this
 313 model, detachment of the nanoparticles from the cell wall is neglected, as it was not observed
 314 under the tested conditions. The corresponding variation in SWCNT concentration, $[\mathbf{SWCNT}]$,
 315 can be modeled with the following system of equations:

316

$$317 \quad \frac{\partial [\mathbf{SWCNT}]_{buffer}}{\partial t} = -k_{ads} [\mathbf{SWCNT}]_{buffer} ([\mathbf{SWCNT}]_{max} - [\mathbf{SWCNT}]_{bound}) \quad (2)$$

$$318 \quad \frac{\partial [\mathbf{SWCNT}]_{bound}}{\partial t} = k_{ads} [\mathbf{SWCNT}]_{buffer} ([\mathbf{SWCNT}]_{max} - [\mathbf{SWCNT}]_{bound})$$

$$319 \quad -k_{in} [\mathbf{SWCNT}]_{bound} \quad (3)$$

320
$$\frac{\partial[\text{SWCNT}]_{in}}{\partial t} = k_{in}[\text{SWCNT}]_{bound} \quad (4)$$

321 where $[\text{SWCNT}]_{max}$ is the maximum concentration of SWCNTs that can be accommodated by the
322 surface of the cells. The kinetic parameters in Equations 2-4 were determined by fitting the model
323 to the time-traces of SWCNT NIR-fluorescence shown in **Figure 2b** (see “Computational
324 modeling” section in the SI for model details). The calculated best-fit rate constants for SWCNT
325 adsorption and internalization in cyanobacteria were compared to the values obtained by Au *et al.*,
326 who applied an analogous two-step model to describe nanoparticle transport in tumor cells⁶¹.
327 While the resulting best-fit rate constant for SWCNT-adsorption, $k_{ads} = (9.08 \pm 0.16) \times 10^{-8} \text{ s}^{-1}$,
328 differed substantially from the values reported for tumor cells, the internalization rate constant, k_{in}
329 $= (1.466 \pm 0.011) \times 10^{-4} \text{ s}^{-1}$, was in close agreement to what had previously reported for
330 nanoparticle internalization, $(1.7 \pm 0.1) \times 10^{-4} \text{ s}^{-1}$. This discrepancy is indicative of the
331 fundamentally different adsorption mechanism in *Synechocystis* cells compared to mammalian
332 systems.

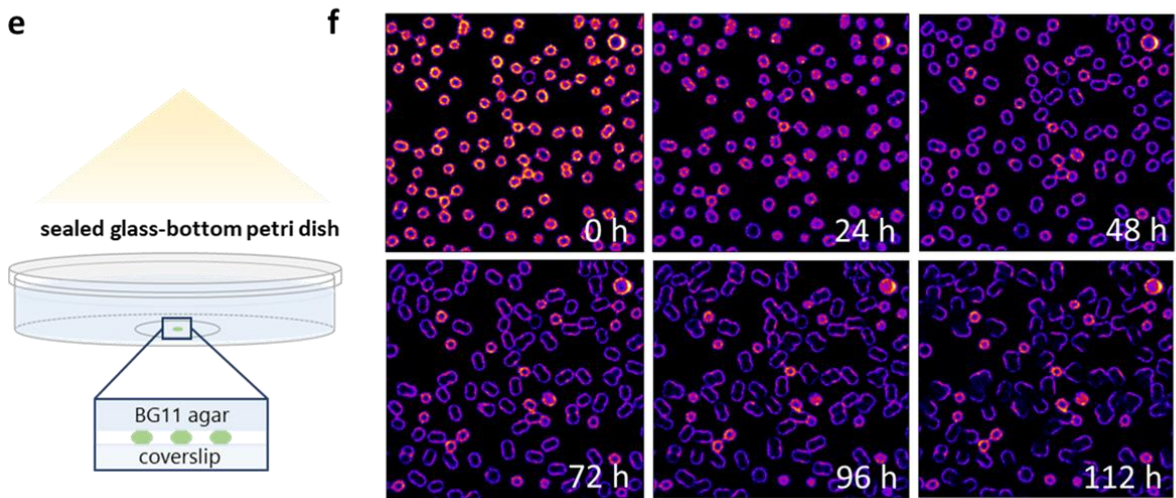
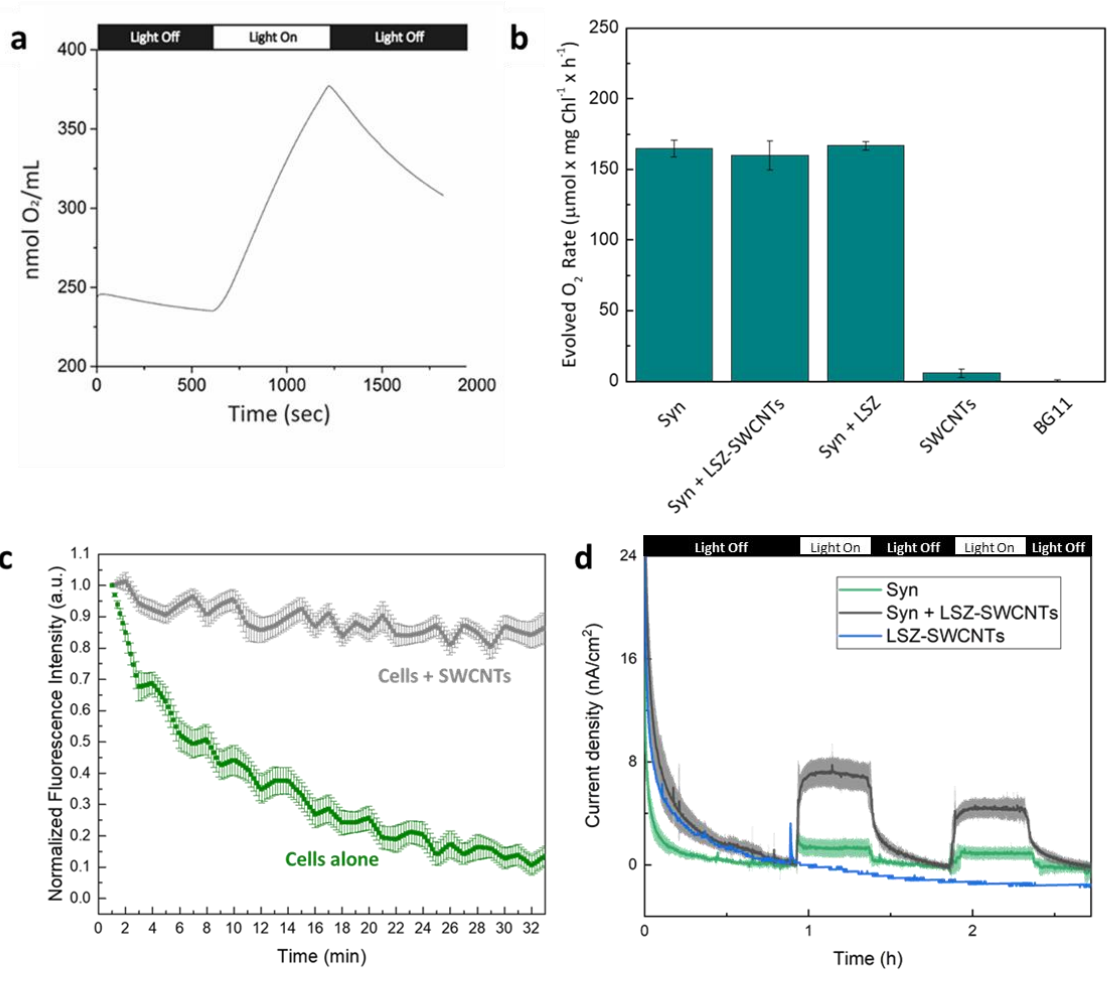
333 Following internalization, we examined the effects of the SWCNTs on cell viability by comparing
334 the oxygen evolution of cells in the presence and absence of LSZ-SWCNTs (**Figure 5**).
335 Photosynthesis and respiration, which are, respectively, oxygen-evolving and -consuming
336 processes, occur simultaneously when photosynthetic cells are illuminated. Photosynthetic activity
337 of *Synechocystis* cells incubated with LSZ-SWCNTs was confirmed by continuous, light-
338 dependent oxygen evolution over a 10-minute interval (**Figure 5a**). Cells incubated in the presence
339 of LSZ-SWCNTs showed no significant difference in the oxygen evolution rate compared to
340 control cells (in the absence of LSZ-SWCNTs) under the conditions tested (**Figure 5b**). We further
341 examined the effects of SWCNT properties across the accelerated lifespan of cells undergoing
342 photobleaching. Compared to autofluorescent cell pigments, which undergo rapid photobleaching

343 upon continuous exposure to high-power 780 nm excitation (**Figure 5c**), the nanobionic cells
344 incubated with LSZ-SWCNTs show enhanced NIR photostability under continuous illumination,
345 sustaining over 95% of the initial NIR fluorescence intensity over 30 minutes.

346 Cell viability over ten days was further verified by growth experiments, where the majority of cells
347 treated with LSZ-SWCNTs (ca 75%) were shown to retain normal growth characteristics and cell
348 morphology (**Figure 5a-c and S9-10**). Furthermore, the nanobionic cells demonstrate enhanced
349 photo-exoelectrogenicity, as shown in the chronoamperometry (CA) measurements presented in
350 **Figure 5d**. Prior to illumination, all electrodes exhibited an initial drop in current that was
351 attributed to diffusion-limited extraction of capacitive charge. Upon cyclic light-dark periods, the
352 microbes show a reversible photo-response. Notably, within the first illumination cycle, the
353 electrode composed of SWCNT-treated *Synechocystis* cells exhibited up to a seven-fold
354 enhancement of the photocurrent density, reaching 7 nA/cm² under 100 μmol photons m⁻² s⁻¹
355 illumination, compared to 1 nA/cm² for untreated cells under the same conditions. The current
356 from the untreated *Synechocystis* cells remained lower than that of the SWCNT-treated cells in the
357 second illumination cycle. Increases in current output were visible only in samples containing
358 cyanobacteria, while no photo-response was observed when the electrode surface was modified
359 with LSZ-SWCNTs alone. Therefore, the increased photo-current is attributed to enhanced
360 photosynthetic charge generation and/or extraction from the microbes rather than the LSZ-
361 SWCNTs themselves.

362 SWCNT distribution before and after cell division was studied using time-lapse *in vivo* cell
363 imaging *via* confocal NIR fluorescence microscopy. *Synechocystis* cells were immobilized onto
364 poly-lysine coated petri dishes, incubated for 1 hour with LSZ-SWCNTs, washed with HEPES
365 buffer to eliminate excess nanoparticles, and covered with 5 mL of warm 1% agar in BG11 to

366 enable sustained growth while restricting movement of the specimen (**Figure 5e**). Cells were
367 continually illuminated by white light ($20 \mu\text{mol photons m}^{-2} \text{s}^{-1}$) for growth, and SWCNTs were
368 imaged using 780 nm excitation. Confocal fluorescence images showed that the majority (*ca* 70%)
369 of the *Synechocystis* cells exhibited sustained growth and cell division for more than 100 hours
370 following treatment with LSZ-SWCNTs (**Figure 5f and Figure S10**). A closer look at the
371 nanoparticle distribution following division revealed that a portion of the SWCNTs originally
372 incorporated within the original cells are transferred to the daughter cells. Although the bulk NIR
373 fluorescence remained constant (**Figure 5c**), we noticed a heterogeneity in NIR fluorescence
374 distribution over time on the single-cell level; cells that did not undergo division displayed higher
375 NIR fluorescence intensities over the course of the experiment. We attributed the observed higher
376 intensities to entrapped SWCNTs that could not migrate to newly formed daughter cells, as well
377 as to a trace increase in NIR autofluorescence that arises from dying photosynthetic cells (see also
378 **Figure S4**). The distinctive intensities can therefore optically distinguish dividing and non-
379 dividing cells through NIR imaging.



382 **Figure 5 | Effect of SWCNT Internalization on Photosynthesis and Cell Viability.** (a) A representative plot of
383 dissolved oxygen concentration in a *Synechocystis* culture in the presence of 10 mg/L LSZ-SWCNTs. Samples were
384 illuminated with white light at $200 \mu\text{mol photons m}^{-2} \text{s}^{-1}$. (b) Net oxygen production rate of illuminated *Synechocystis*
385 cells in the absence and presence of LSZ-SWCNTs. Control measurements were taken for LSZ-SWCNTs in BG11
386 medium and medium only. Measurements were normalized by chlorophyll content and are based on three independent
387 experiments. (c) Average NIR fluorescence emission of cells normalized by their initial intensities with (grey line,
388 980 nm long-pass emission filter) and without LSZ-SWCNTs (green line, 800 nm long-pass emission filter) over time
389 upon continuous illumination at 780 nm with 31 mW/cm^2 power. (d) Directed photo-response of *Synechocystis*
390 (green) and *Synechocystis*-LSZ-SWCNT composite (gray) on ITO electrodes measured in PB medium. The blue curve
391 represents the light-response of LSZ-SWCNT modified ITO in the absence of *Synechocystis* cells. (e) Schematic of
392 the glass-bottom petri dish used to monitor cyanobacterial growth on the microscope stage. Cells are immobilized
393 onto a poly-lysine-coated coverslip and covered by a thick layer of 1% agar in BG11. Dishes were sealed to minimize
394 evaporation. (f) NIR confocal fluorescence images of *Synechocystis* cells treated with LSZ-SWCNTs and grown on
395 1% agar in BG11 (excitation at 780 nm, emission above 980 nm).

396 **3. Conclusions**

397 Nanobionic SWCNT applications thus far have largely focused on augmenting light-harvesting or
398 biochemical detection capabilities of extracted organelles or leaf lamina from plants. The study
399 presented herein offers an uncharted exploration of nanobionic applications based on living
400 prokaryotic cells. These nanobionic cells show a persisting, augmented fluorescence that extends
401 beyond the visible fluorescence limits of the cell, enabling long-term, optical imaging in
402 autofluorescent living systems. In contrast to previously studied systems, where internalization
403 was observed in the presence of functionalized SWCNTs with both positive or negative zeta
404 potentials, cyanobacterial cells demand more stringent engineering design rules, requiring
405 SWCNTs to possess strongly positive zeta potentials in order to traverse the surrounding wall of
406 the cell. We apply this design rule to demonstrate nanotube-facilitated protein delivery within a

407 cell that is otherwise largely impenetrable to even the cell lysis protein, lysozyme, under the same
408 conditions. Though the successful conjugative methods demonstrated herein are restricted to
409 protein-functionalized SWCNTs, the internalization of both active and inactive protein conjugates
410 suggests that synthetic functionalization with suitable charge distributions may also be used for
411 nanoparticle uptake.

412 In addition to fundamental mechanisms of prokaryotic nanoparticle uptake and protein delivery,
413 we demonstrate the application of SWCNT-based nanobionics for enhancing bio-photovoltaic
414 devices and for cross-generational imaging. Although the precise mechanism for bio-photovoltaic
415 improvement remains an ongoing going area of research, we attribute the enhancement to either
416 improved charge extraction from the metallic SWCNTs or light-harvesting from the
417 semiconducting SWCNTs. Furthermore, the unprecedented application of NIR confocal
418 fluorescence microscopy allows real-time, cross-generational monitoring of a length-dependent,
419 heterogeneous accumulation of SWCNTs that has otherwise been overlooked with conventional
420 widefield NIR microscopy. While the majority of SWCNTs remain along the peripheral regions,
421 SWCNTs are shown to access the cytosol, where chromosomal and plasmid DNA are accessible,
422 opening the doors to further applications to gene delivery in addition to the protein delivery that
423 has been demonstrated herein. Furthermore, daughter cells are shown to inherit nanobionic
424 capabilities imparted by the nanotubes, which has been used in this study for cross-generational
425 NIR cell tracking of live and dead cells. We have demonstrated the synthetic augmentation of
426 living organisms across several generations in the absence of any genetic manipulation. This
427 demonstration of inherited nanobionics opens the doors to new possibilities to engineering living,
428 dividing cells with capabilities that extend beyond those found in Nature.

429

430

431 **4. Methods**

432 **Noncovalent Functionalization of SWCNTs.** The SWCNTs used in this study were purified
433 HiPco nanotubes (NanoIntegris, Lot. No. HP26-019) with a diameter of 0.8 – 1.2 nm and a length
434 of 100-1000 nm. SWCNTs were wrapped with a (AT)₁₅ oligonucleotide (Eurofins Genomics)
435 following a modified protocol from Zheng *et al*⁶⁴, and with chitosan (Carl Roth) as described in
436 Reuel *et al*⁶⁵. To summarize, 1 mg of SWCNTs was suspended in either deionized water or, in the
437 case of chitosan, 1% acetic acid to yield a final concentration of 1 mg/mL. Samples were sonicated
438 using a cup-horn sonicator (140 mm, Qsonica, LLC) for 90 minutes at 1% amplitude in an ice bath.
439 The sonicated SWCNT suspension was centrifuged (Eppendorf Centrifuge 5424 R) for 180
440 minutes at 16500 x g to pellet SWCNT aggregates. The suspensions were dialyzed against 2 L of
441 deionized water using either a 14 kDa MWCO cellulose membrane (Sigma Aldrich), in the case
442 of DNA-SWCNTs, or a 300 kDa MWCO cellulose membrane, in the case of chitosan-SWCNTs.
443 LSZ-, HST- and BSA-SWCNTs were prepared following a similar protocol by suspending 1 mg
444 of HiPco nanotubes and 5 mg of lysozyme from chicken egg white (Sigma Aldrich), 10 mg histone
445 type-III_S (Sigma Aldrich), or 10 mg of bovine serum albumin (Sigma Aldrich), in 1 mL of 1 mM
446 HEPES buffer (pH 7.4) and sonicating using cup-horn sonication for 90 minutes at 1% amplitude
447 on ice. Unbound protein was removed through dialysis against 2 L of 1 mM HEPES buffer using
448 a 300 kDa MWCO cellulose membrane. The same protocol was used to suspend SWCNTs with
449 thermally deactivated LSZ. However, prior to dialysis, the LSZ solution was heated to 90 °C for
450 20 minutes, as described by Xie *et al.*³³ SWCNT concentrations were calculated from absorbance
451 measurements at 632 nm in a UV-Vis-NIR scanning spectrometer (Shimadzu 3600 Plus) using an
452 extinction coefficient of 0.036 L/(mg cm). The concentration of functionalized SWCNT

453 suspensions ranged between 80-100 mg/L, except for BSA and HST-SWCNTs suspensions where
454 concentrations between 35-50 mg /L were obtained.

455 **Zeta-potential measurements.** All stock solutions of SWCNTs were diluted in 1 mM HEPES
456 buffer (pH 7.4) to yield a final concentration of 10 mg/L. Zeta potential measurements were carried
457 out with a Zetasizer Nano ZS analyzer from Malvern, using folded capillary cells.

458 **Bacterial strains and growth conditions.** Liquid cultures of wild-type *Synechocystis* and *Nostoc*
459 were grown in BG11 medium (Rippka et al⁶⁶) supplemented with 10 mM TES buffer (pH 8.0) at
460 30°C under 50 $\mu\text{mol photons m}^{-2} \text{ s}^{-1}$ of white light with constant shaking. The Δhfq mutant cells
461 were additionally supplemented with 7 $\mu\text{g/mL}$ of chloramphenicol⁶⁷. At an $\text{OD}_{750\text{nm}}$ of 0.9-1.2,
462 cells from 2 mL of the culture were harvested by centrifugation at 5000 rpm at room temperature.
463 Pellets were washed three times with 1 mM HEPES buffer (pH 7.4) and then re-suspended in the
464 same buffer to achieve a final OD_{750} of 1.4.

465 **NIR fluorescence imaging.** Cells were fixed onto poly-lysine coated glass-bottom petri dishes by
466 spotting 30 μL of the cell suspension at OD_{750} of 1.4 for 10 minutes followed by washing with
467 HEPES. The cells were then covered with 50 μL of 1 mM HEPES buffer (pH 7.4). They were
468 imaged using a custom-built optical setup consisting of an inverted microscope (Eclipse Ti-U,
469 Nikon AG Instruments) with an oil-immersion TIRF 100 x objective (N.A. 1.49, Nikon) coupled
470 to a CREST X-Light spinning-disk confocal imaging system (CREST Optics) (60 μm pinholes)
471 and an InGaAs camera (NIRvana 640 ST, Princeton Instruments). Samples were illuminated using
472 a TriLine LaserBank system (Cairn Research) at 640 nm and 780 nm, and fluorescence was
473 collected using either an 800 nm (Chroma), 980 nm long-pass filters (Semrock), or a 1260 ± 15
474 nm band pass filter (Chroma). Images were acquired using the Nikon NIS-Elements software
475 (Nikon Instruments). 10 μL of SWCNT stock solutions were added to a 50 μL droplet of 1 mM

476 HEPES buffer to yield a final concentration of 2 mg/L. Following incubation, the SWCNT solution
477 was replaced by a 50 μ L droplet of fresh HEPES buffer. SWCNT fluorescence quenching was
478 monitored by adding ferricyanide to yield a final concentration of 120 mM.

479 For the long-term imaging, the cells were covered with 5 mL of warm 1% agar in BG11 after
480 washing with HEPES buffer to eliminate the excess of nanoparticles. Following solidification of
481 the agar the plate was sealed to minimize evaporation. The cells were kept under 20 μ mol photons
482 $\text{m}^{-2} \text{s}^{-1}$ of white light and bright-field images were recorded every 20 minutes for the duration of
483 the experiment. After a day of growth, SWCNT fluorescence was monitored with 780 nm
484 excitation (2.5 mW/cm^2) and a 980 nm long-pass emission filter.

485 **Length Separation of Sodium Deoxycholate-SWCNTs.** Length separation of SWCNTs was
486 achieved by density gradient centrifugation following a modified protocol from Cognet et al.⁶⁸
487 First, 25 mg of purified HiPCo SWCNTs (NanoIntegris, Lot. No. HP29-064) were dispersed in 25
488 mL of 1 wt% sodium deoxycholate solution in deionized water. The dispersion was homogenized
489 for 20 minutes at 5000 rpm (PT 1300D, Polytron) and sonicated for 1 hour using a probe-tip
490 ultrasonicator (1/4 in. tip. Q700 Sonicator, QSonica) at 10% amplitude in ice bath. The SWCNT
491 suspension was centrifuged at 164 000 \times g for 4 hours at 25 $^{\circ}\text{C}$ (Optima XPN-80, SW 32 Ti Rotor,
492 Beckman Coulter). The supernatant was collected and stored at room temperature.

493 Density gradient solutions were prepared by stacking four layers of 3 mL of 60 wt%, 10 wt%, 7.5
494 wt%, and 5 wt% iodixanol solution (OptiPrep, Sigma-Aldrich) from bottom to top in 17 mL
495 polycarbonate centrifugal tubes (Beckman Coulter). A volume of 3 mL stock DOC-SWCNT
496 suspension was added on top of the density-gradient iodixanol solution and centrifuged for 4 hours
497 at 175000 \times g and at a temperature of 4 $^{\circ}\text{C}$ (SW 32 Ti Rotor, Beckman Coulter). Following
498 centrifugation, SWCNTs with different lengths were found distributed along the density gradient,

499 with shorter nanotubes located closer to the top of the centrifugal tube and longer nanotubes
500 towards the bottom of the tube. Twenty fractions (0.5 mL volume) were extracted by manually
501 pipetting from the top to the bottom of the centrifugal tube.

502 **AFM imaging.** A small volume (10 μ L) of length-separated SWCNT fractions was drop-casted
503 on a freshly cleaved mica surface. The sample was rinsed with deionized water several times in
504 order to remove excess surfactant from the surface and dried in air. Morphological characterization
505 was performed using a commercial AFM setup (Cypher, Asylum Research) equipped with a
506 commercial Si cantilever (AC160TSA-R3, Asylum Research). Topography, phase, and amplitude
507 images were acquired in standard tapping mode. SWCNT lengths were evaluated using standard
508 tools (e.g. plane subtraction and profile extraction) featured in the AFM data analysis software
509 (Gwyddion 2.52).

510 **Protein-functionalization of length-separated SWCNTs.** Length-separated DOC-SWCNTs
511 were precipitated according to the literature using methanol⁶⁹. Sedimented SWCNTs were washed
512 using deionized water by centrifugation several times in order to remove unwanted surfactant and
513 iodixanol residues retained from the density gradient ultracentrifugation procedure. Following
514 these washing steps, SWCNTs were mixed with 0.3 mL of lysozyme solution (5 mg/mL) in
515 deionized water and bath sonicated for 15 minutes. The suspension was then sonicated with a cup
516 horn sonicator (1% amplitude) for 1.5 hours. The samples were centrifuged at 16500 g for 3 hours
517 to remove SWCNT aggregates.

518 **Raman Characterization.** Raman spectra were recorded at an excitation wavelength of 532 nm
519 from 200 to 1800 cm^{-1} using a water-immersion 63x objective (0.90 N.A) on a confocal
520 spectroscope (inVia Raman Microscope, Renishaw). For automatic confocal Raman mapping,
521 confocal Raman spectra were recorded with a step size $< 1 \mu\text{m}$ in X-Y, for a total number of 9x9

522 spectra. Spectra were automatically acquired along the Z direction, where Z= 0 corresponds to the
523 higher contrast of the cell on a bright-field image. The spectrometer was calibrated before
524 measurements using an internal standard. 3D maps were generated using a Matlab script (Matlab
525 R2015, Mathworks).

526 **TEM and Immunogold Labeling.** Following a 1-hour incubation with either 2 mg/L LSZ-
527 SWCNTs (positive control) or with 5 mg/mL lysozyme solution (negative control), *Synechocystis*
528 cells were fixed with 2% paraformaldehyde and 0.2% glutaraldehyde in 0.1 M cacodylate buffer
529 pH 7.2 for 2 h. After washing with 0.1 M cacodylate buffer, pH 7.2, cells were dehydrated with
530 dimethylformamide (DMF) at increasing concentrations (50%, 75%, and 90%). Cells were
531 embedded in Lowicryl K4M resin (Emsdium, Hatfield, PA, USA), and samples were then placed
532 in gelatin capsules and polymerized at -20°C overnight by UV irradiation at $\lambda = 360$ nm.

533 Ultrathin sections (60 nm) were subsequently cut with a PT-PC PowerTome ultramicrotome
534 (RMC, Tucson, Arizona USA). The sections were collected on nickel grids and were blocked with
535 PBS with 0.15% glycine for 5 minutes, followed by 0.4% gelatin in a solution of 0.1% BSA in
536 PBS. Samples were then incubated overnight with the primary antibody, antilysozyme (ab391,
537 Abcam, Cambridge, United Kingdom), at 1:100 dilution in PBS with 1% BSA. After washing with
538 PBS with 0.1% BSA, the grids were incubated with the secondary antibody, gold particle-
539 conjugated (10nm) protein A, in PBS with 4% BSA. After extensive washing, the samples were
540 imaged using a HT7700 TEM (Hitachi, Tokyo, Japan).

541 **Determination of the *chlorophyll a* content.** The chlorophyll *a* content was used to normalize
542 the oxygen evolution and consumption rates. Cells were pelleted for 7 min at 15000 x g and then
543 re-suspended in 1 mL of 99% methanol, pre-cooled at 4°C. The samples were incubated at 4°C for
544 20 min in the dark and soluble pigments were separated from cell debris by centrifugation for 7

545 min at 15000 x g at 4°C. Chlorophyll *a* content was determined according to the equation Chl_a
546 [µg/mL] = 12.9447 (A₆₆₄-A₇₂₀) as described by Ritchie 2006⁷⁰.

547 **Measuring net oxygen production and consumption rates under light and dark conditions.**

548 Cells were harvested during the late exponential growth phase (OD > 1) by centrifugation and re-
549 suspended in fresh BG-11 medium to an OD₇₅₀ of 1.4. The oxygen concentration under light and
550 dark conditions for whole cells was monitored at 30°C using a Clark-type electrode (Hansatech,
551 OxyLab+, Norfolk). Samples were illuminated at an intensity of 200 µmol photons m⁻² s⁻¹ under
552 white light. 10 mM of sodium bicarbonate (NaHCO₃) was added to the cell suspensions in the
553 reaction chamber prior to oxygen measurement to provide the cells with an excess carbon source.

554 **Preparation of the electrodes.** ITO-coated PET substrates with an area of 2 cm² (Sigma-Aldrich)

555 were sonicated in ethanol and deionized water (10 minutes each) at room temperature to remove
556 possible impurities. These substrates were then treated for 1 hour with 300 µL of poly-L-lysine
557 solution (0.01 % (w/v), Sigma-Aldrich), followed by washing with deionized water. Wild-type
558 *Synechocystis* cells were grown in BG11 medium to an OD_{750nm} of 3. The cells were pelleted by
559 centrifugation at 5000 rpm for 5 minutes, washed twice with 1 mM HEPES buffer (pH 7.4), and
560 re-suspended in the same buffer to reach a final OD_{750nm} of 2. Finally, 20 µL of the cell suspension
561 were drop-casted onto the poly-L-lysine treated ITO electrodes (active surface of 0.25 cm²) and
562 incubated at 30 °C for 1 hour in dark conditions. *Synechocystis*-modified ITO electrodes were
563 covered with a 14 kDa MWCO dialysis membrane (Sigma-Aldrich), previously soaked in HEPES
564 for 1 hour, and placed at the bottom of a three-electrode electrochemical cell. Electrodes containing
565 LSZ-SWCNTs-modified cells were prepared following a similar procedure: after washing with 1
566 mM HEPES, *Synechocystis* cells were re-suspended in 1 mM HEPES solution containing LSZ-

567 SWCNTs (10 mg/L), drop-casted on the ITO substrates, and incubated for 1 hour at 30 °C. The
568 samples were transferred to the electrochemical cell for photo-response measurements.

569 **Photo-response measurements.** *Synechocystis*-modified ITO electrodes were inserted in a
570 conventional three-electrode electrochemical cell containing a phosphate buffer (PB) solution and
571 equipped with a Pt wire counter-electrode and a standard Ag/AgCl (sat. KCl) reference electrode.
572 The cell was connected to a PalmSens4 potentiostat (PalmSens BV) equipped with PStTrace
573 software. The photo-response was studied performing chronoamperometry (CA) measurements at
574 an applied potential of 300 mV. The current was continuously monitored during dark-light cycles
575 for 3 hours. In particular, the system was stabilized in the dark for 1 hour, followed by two cycles
576 of ~30-minute illumination with a LED light at $100 \mu\text{mol photons m}^{-2} \text{ s}^{-2}$ and 30 minutes of
577 incubation in the dark. Measurements were taken for *Synechocystis*-, SWCNT/*Synechocystis*- and
578 control SWCNT-modified ITO electrodes.

579 **Computational Methods**

580 Model parameters were determined by fitting numerical solutions of the three differential
581 equations to experimental data. The fit between the model and experimental data was achieved
582 with a Matlab (MathWorks) script by using the OPTI toolbox⁷¹. A built-in ODE function, ode45,
583 was used for numerical integration. Additional details are provided in the Supplementary
584 Information under the section “Computational modeling”.

585 **Statistical analyses and Image Processing.** All data points and error bars shown in the figures
586 represent mean values with standard deviations. One-way ANOVA tests were used to evaluate
587 statistically significant differences in oxygen evolution rates. A sample size of n=3 was used for
588 the calculations. Statistical significance was assumed at p-value < 0.05. Z-stacked images of the
589 cells were visualized using a Matlab script. Background subtraction was performed with Fiji-

590 ImageJ for all microscopy images, and an additional median filter (pixel radius = 2) was applied
591 to images shown in **Figure S6** for noise removal.

592 **5. Acknowledgments**

593 The authors are thankful for support from the Swiss National Science Foundation (SNSF) Assistant
594 Professor (AP) Energy Grant. The authors also thank Prof. Kevin Sivula from the Laboratory for
595 Molecular Engineering of Optoelectronic Nanomaterials (LIMNO) at EPFL for granting access to
596 the AFM facility.

597

598 **6. References**

- 599 (1) Liu, Z.; Tabakman, S. M.; Chen, Z.; Dai, H. Preparation of Carbon Nanotube Bioconjugates for
600 Biomedical Applications. *Nat. Protoc.* **2009**, *4* (9), 1372–1381.
- 601 (2) Wang, X.; Liu, Z. Carbon Nanotubes in Biology and Medicine: An Overview. *Chinese Sci. Bull.*
602 **2012**, *57* (2-3), 167–180.
- 603 (3) Hashida, Y.; Tanaka, H.; Zhou, S.; Kawakami, S.; Yamashita, F.; Murakami, T.; Umeyama, T.;
604 Imahori, H.; Hashida, M. Photothermal Ablation of Tumor Cells Using a Single-Walled Carbon
605 Nanotube-Peptide Composite. *J. Control. Release* **2014**, *173* (1), 58–66.
- 606 (4) Jena, P. V.; Shamay, Y.; Shah, J.; Roxbury, D.; Paknejad, N.; Heller, D. A. Photoluminescent
607 Carbon Nanotubes Interrogate the Permeability of Multicellular Tumor Spheroids. *Carbon N. Y.*
608 **2016**, *97*, 99–109.
- 609 (5) Boghossian, A. A.; Zhang, J.; Barone, P. W.; Reuel, N. F.; Kim, J. H.; Heller, D. A.; Ahn, J. H.;
610 Hilmer, A. J.; Rwei, A.; Arkalgud, J. R.; et al. Near-Infrared Fluorescent Sensors Based on Single-
611 Walled Carbon Nanotubes for Life Sciences Applications. *ChemSusChem* **2011**, *4* (7), 848–863.
- 612 (6) Heller, D. A.; Jin, H.; Martinez, B. M.; Patel, D.; Miller, B. M.; Yeung, T.-K.; Jena, P. V.;
613 Höbartner, C.; Ha, T.; Silverman, S. K.; et al. Multimodal Optical Sensing and Analyte Specificity
614 Using Single-Walled Carbon Nanotubes. *Nat. Nanotechnol.* **2009**, *4* (2), 114–120.
- 615 (7) Zubkovs, V.; Schuergers, N.; Lambert, B.; Ahunbay, E.; Boghossian, A. A. Mediatorless,
616 Reversible Optical Nanosensor Enabled through Enzymatic Pocket Doping. *Small* **2017**, *13* (42),
617 1–10.
- 618 (8) Gillen, A. J.; Kupis-Rozmyslowicz, J.; Gigli, C.; Schürgers, N.; Boghossian, A. A. Xeno Nucleic
619 Acid Nanosensors for Enhanced Stability Against Ion-Induced Perturbations. *J. Phys. Chem. Lett.*
620 **2018**, 4336–4343.

- 621 (9) Bachilo, S. M.; Strano, M. S.; Kittrell, C.; Hauge, R. H.; Smalley, R. E.; Weisman, R. B.
622 Structure-Assigned Optical Spectra of Single-Walled Carbon Nanotubes. *Science* (80-.). **2002**,
623 298 (5602), 2361–2366.
- 624 (10) Barone, P. W.; Baik, S.; Heller, D. A.; Strano, M. S. Near-Infrared Optical Sensors Based on
625 Single-Walled Carbon Nanotubes. *Nat. Mater.* **2005**, 4 (1), 86–92.
- 626 (11) Holt, B. D.; Dahl, K. N.; Islam, M. F.; Al, H. E. T. Cells Take up and Recover from Nanotubes
627 with Two Distinct Rates. *ACS Nano* **2012**, 6 (4), 3481–3490.
- 628 (12) Boyer, P.; Ganesh, S.; Qin, Z.; Holt, B. D.; Buehler, M. J.; Islam, M. F.; Dahl, K. N. Delivering
629 Single-Walled Carbon Nanotubes to the Nucleus Using Engineered Nuclear Protein Domains.
630 *ACS Appl. Mater. Interfaces* **2016**, 8 (5), 3524–3534.
- 631 (13) Giraldo, J. P.; Landry, M. P.; Faltermeier, S. M.; McNicholas, T. P.; Iverson, N. M.; Boghossian,
632 A. A.; Reuel, N. F.; Hilmer, A. J.; Sen, F.; Brew, J. a; et al. Plant Nanobionics Approach to
633 Augment Photosynthesis and Biochemical Sensing. *Nat. Mater.* **2014**, 13 (4), 400–408.
- 634 (14) Wong, M. H.; Giraldo, J. P.; Kwak, S.-Y.; Koman, V. B.; Sinclair, R.; Lew, T. T. S.; Bisker, G.;
635 Liu, P.; Strano, M. S. Nitroaromatic Detection and Infrared Communication from Wild-Type
636 Plants Using Plant Nanobionics. *Nat. Mater.* **2016**, 16, 1–8.
- 637 (15) Wong, M. H.; Misra, R. P.; Giraldo, J. P.; Kwak, S. Y.; Son, Y.; Landry, M. P.; Swan, J. W.;
638 Blankschtein, D.; Strano, M. S. Lipid Exchange Envelope Penetration (LEEP) of Nanoparticles for
639 Plant Engineering: A Universal Localization Mechanism. *Nano Lett.* **2016**, 16 (2), 1161–1172.
- 640 (16) Pogodin, S.; Baulin, V. A. Can a Carbon Nanotube Pierce through a Phospholipid Bilayer? *ACS*
641 *Nano* **2010**, 4 (9), 5293–5300.
- 642 (17) Pogodin, S.; Slater, N. K. H.; Baulin, V. A. Surface Patterning of Carbon Nanotubes Can Enhance
643 Their Penetration through a Phospholipid Bilayer. *ACS Nano* **2011**, 5 (2), 1141–1146.
- 644 (18) Lacerda, L.; Russier, J.; Pastorin, G.; Herrero, M. A.; Venturelli, E.; Dumortier, H.; Al-Jamal, K.
645 T.; Prato, M.; Kostarelos, K.; Bianco, A. Translocation Mechanisms of Chemically Functionalised
646 Carbon Nanotubes across Plasma Membranes. *Biomaterials* **2012**, 33 (11), 3334–3343.
- 647 (19) Kostarelos, K.; Lacerda, L.; Pastorin, G.; Wu, W.; Wieckowski, S.; Luangsivilay, J.; Godefroy, S.;
648 Pantarotto, D.; Briand, J.-P.; Muller, S.; et al. Cellular Uptake of Functionalized Carbon
649 Nanotubes Is Independent of Functional Group and Cell Type. *Nat. Nanotechnol.* **2007**, 2 (2),
650 108–113.
- 651 (20) Ulissi, Z. W.; Sen, F.; Gong, X.; Sen, S.; Iverson, N.; Boghossian, A. A.; Godoy, L. C.; Wogan, G.
652 N.; Mukhopadhyay, D.; Strano, M. S. Spatiotemporal Intracellular Nitric Oxide Signaling
653 Captured Using Internalized, near-Infrared Fluorescent Carbon Nanotube Nanosensors. *Nano Lett.*
654 **2014**, 14 (8), 4887–4894.
- 655 (21) Giraldo, J. P.; Landry, M. P.; Kwak, S.-Y.; Jain, R. M.; Wong, M. H.; Iverson, N. M.; Ben-Naim,
656 M.; Strano, M. S. A Ratiometric Sensor Using Single Chirality Near-Infrared Fluorescent Carbon
657 Nanotubes: Application to In Vivo Monitoring. *Small* **2015**.

- 658 (22) Holt, B. D.; Dahl, K. N.; Islam, M. F. Quantification of Uptake and Localization of Bovine Serum
659 Albumin-Stabilized Single-Wall Carbon Nanotubes in Different Human Cell Types. *Small* **2011**, *7*
660 (16), 2348–2355.
- 661 (23) Hoiczky, E.; Hansel, A. Cyanobacterial Cell Walls: News from an Unusual Prokaryotic Envelope.
662 *J. Bacteriol.* **2000**, *182* (5), 1191–1199.
- 663 (24) Sleytr, U. B.; Schuster, B.; Egelseer, E. M.; Pum, D. S-Layers: Principles and Applications. *FEMS*
664 *Microbiol. Rev.* **2014**, *38* (5), 823–864.
- 665 (25) Vioque, A. Transformation of Cyanobacteria. *Adv. Exp. Med. Biol.* **2007**, *616*, 12–22.
- 666 (26) Demirer, G. S.; Zhang, H.; Matos, J. L.; Goh, N. S.; Cunningham, F. J.; Sung, Y.; Chang, R.;
667 Aditham, A. J.; Chio, L.; Cho, M.-J.; et al. High Aspect Ratio Nanomaterials Enable Delivery of
668 Functional Genetic Material without DNA Integration in Mature Plants. *Nat. Nanotechnol.* **2019**,
669 *14*, 456–464.
- 670 (27) Kwak, S.-Y.; Lew, T. T. S.; Sweeney, C. J.; Koman, V. B.; Wong, M. H.; Bohmert-Tatarev, K.;
671 Snell, K. D.; Seo, J. S.; Chua, N.-H.; Strano, M. S. Chloroplast-Selective Gene Delivery and
672 Expression in Planta Using Chitosan-Complexed Single-Walled Carbon Nanotube Carriers. *Nat.*
673 *Nanotechnol.* **2019**, *14*, 447–455.
- 674 (28) Lew, T. T. S.; Wong, M. H.; Kwak, S. Y.; Sinclair, R.; Koman, V. B.; Strano, M. S. Rational
675 Design Principles for the Transport and Subcellular Distribution of Nanomaterials into Plant
676 Protoplasts. *Small* **2018**, *14* (44), 1–13.
- 677 (29) Sekar, N.; Umasankar, Y.; Ramasamy, R. P. Photocurrent Generation by Immobilized
678 Cyanobacteria via Direct Electron Transport in Photo-Bioelectrochemical Cells. *Phys. Chem.*
679 *Chem. Phys.* **2014**, *16* (17), 7862–7871.
- 680 (30) Stavrinidou, E.; Gabrielsson, R.; Gomez, E.; Crispin, X.; Nilsson, O.; Simon, D. T.; Berggren, M.
681 Electronic Plants. *Sci. Adv.* **2015**, *1* (10), e1501136.
- 682 (31) Bomboi, F.; Bonincontro, a.; La Mesa, C.; Tardani, F. Interactions between Single-Walled Carbon
683 Nanotubes and Lysozyme. *J. Colloid Interface Sci.* **2011**, *355* (2), 342–347.
- 684 (32) Nepal, D.; Geckeler, K. E. PH-Sensitive Dispersion and Debundling of Single-Walled Carbon
685 Nanotubes: Lysozyme as a Tool. *Small* **2006**, *2* (3), 406–412.
- 686 (33) Xie, L.; Chou, S. G.; Pande, A.; Pande, J.; Zhang, J.; Dresselhaus, M. S.; Kong, J.; Liu, Z. Single-
687 Walled Carbon Nanotubes Probing the Denaturation of Lysozyme. *J. Phys. Chem. C* **2010**, *114*
688 (17), 7717–7720.
- 689 (34) Horn, D. W.; Tracy, K.; Easley, C. J.; Davis, V. A. Lysozyme Dispersed Single-Walled Carbon
690 Nanotubes: Interaction and Activity. *J. Phys. Chem. C* **2012**, *116* (18), 10341–10348.
- 691 (35) Horn, D. W.; Ao, G.; Maugey, M.; Zakri, C.; Poulin, P.; Davis, V. A. Dispersion State and Fiber
692 Toughness: Antibacterial Lysozyme-Single Walled Carbon Nanotubes. *Adv. Funct. Mater.* **2013**,
693 *23* (48), 6082–6090.

- 694 (36) Nepal, D.; Minus, M. L.; Kumar, S. Lysozyme Coated DNA and DNA/SWNT Fibers by Solution
695 Spinning. *Macromol. Biosci.* **2011**, *11* (7), 875–881.
- 696 (37) Nyankima, A. G.; Horn, D. W.; Davis, V. A. Free-Standing Films from Aqueous Dispersions of
697 Lysozyme, Single-Walled Carbon Nanotubes, and Polyvinyl Alcohol. *ACS Macro Lett.* **2014**, *3*,
698 77–79.
- 699 (38) Lee, Y.; Geckeler, K. E. Cytotoxicity and Cellular Uptake of Lysozyme-Stabilized Gold
700 Nanoparticles. *J. Biomed. Mater. Res. - Part A* **2012**, *100 A* (4), 848–855.
- 701 (39) Holt, B. D.; McCorry, M. C.; Boyer, P. D.; Dahl, K. N.; Islam, M. F. Not All Protein-Mediated
702 Single-Wall Carbon Nanotube Dispersions Are Equally Bioactive. *Nanoscale* **2012**, 7425–7434.
- 703 (40) Zubkovs, V.; Antonucci, A.; Schuergers, N.; Lambert, B.; Latini, A.; Ceccarelli, R.; Santinelli, A.;
704 Rogov, A.; Ciepielewski, D.; Boghossian, A. A. Spinning-Disc Confocal Microscopy in the
705 Second near-Infrared Window (NIR-II). *Sci. Rep.* **2018**, *8* (1), 1–10.
- 706 (41) Heller, D. A.; Mayrhofer, R. M.; Baik, S.; Grinkova, Y. V.; Usrey, M. L.; Strano, M. S.
707 Concomitant Length and Diameter Separation of Single-Walled Carbon Nanotubes. *J. Am. Chem.*
708 *Soc.* **2004**, *126* (44), 14567–14573.
- 709 (42) Rajan, A.; Strano, M. S.; Heller, D. A.; Hertel, T.; Schulten, K. Length-Dependent Optical Effects
710 in Single Walled Carbon Nanotubes. *J. Phys. Chem. B* **2008**, *112* (19), 6211–6213.
- 711 (43) Boyer, P. D.; Dahl, N. Length-Dependent Intracellular Bundling of Single-Walled Carbon
712 Nanotubes Influences. *J. Mater. Chem. B* **2017**, *5*, 6657–6665.
- 713 (44) Kang, B.; Chang, S.; Dai, Y.; Yu, D.; Chen, D. Cell Response to Carbon Nanotubes: Size-
714 Dependent Intracellular Uptake Mechanism and Subcellular Fate. *Small* **2010**, *6* (21), 2362–2366.
- 715 (45) Becker, M. L.; Fagan, J. A.; Gallant, N. D.; Bauer, B. J.; Bajpai, V.; Hobbie, E. K.; Lacerda, S. H.;
716 Migler, K. B.; Jakupciak, J. P. Length-Dependent Uptake of DNA-Wrapped Single-Walled
717 Carbon Nanotubes. *Adv. Mater.* **2007**, *19* (7), 939–945.
- 718 (46) Barone, P. W.; Parker, R. S.; Strano, M. S. In Vivo Fluorescence Detection of Glucose Using a
719 Single-Walled Carbon Nanotube Optical Sensor: Design, Fluorophore Properties, Advantages, and
720 Disadvantages. *Anal. Chem.* **2005**, *77* (23), 7556–7562.
- 721 (47) Robinson, S. J.; Deroo, C. S.; Yocum, C. F. Photosynthetic Electron Transfer in Preparations of
722 the Cyanobacterium *Spirulina Platensis*. *Plant Physiol.* **1982**, *70* (1), 154–161.
- 723 (48) Clark, M. G.; Patrick, E. J.; Pattern, G. S.; Crane, F. L.; Low, H.; Grebing, C. Evidence for the
724 Extracellular Reduction of Ferricyanide by Rat Liver. A Transplasma Membrane Redox System.
725 *Biochem. J.* **1996**, *200*, 565–572.
- 726 (49) Mehta, K. K.; Evitt, N. H.; Swartz, J. R. Chemical Lysis of Cyanobacteria. *J. Biol. Eng.* **2015**, *9*
727 (1), 1–8.

- 728 (50) Williams, J. G. K. Construction of Specific Mutations in Photosystem II Photosynthetic Reaction
729 Center by Genetic Engineering Methods in *Synechocystis* 6803. *Methods Enzymol.* **1988**, *167*,
730 766–778.
- 731 (51) Trautner, C.; Vermaas, W. F. J. The *sll1951* Gene Encodes the Surface Layer Protein of
732 *Synechocystis* Sp. Strain PCC 6803. *J. Bacteriol.* **2013**, *195* (23), 5370–5380.
- 733 (52) Neves, V.; Heister, E.; Costa, S.; Tilmaciu, C.; Borowiak-Palen, E.; Giusca, C. E.; Flahaut, E.;
734 Soula, B.; Coley, H. M.; McFadden, J.; et al. Uptake and Release of Double-Walled Carbon
735 Nanotubes by Mammalian Cells. *Adv. Funct. Mater.* **2010**, *20* (19), 3272–3279.
- 736 (53) Ibrahim, H. R. On the Novel Catalytically-Independent Antimicrobial Function of Hen Egg-White
737 Lysozyme: A Conformation-Dependent Activity. *Nahrung* **1998**, *42* (3-4), 187–193.
- 738 (54) Henriques, S. T.; Melo, M. N.; Castanho, M. A. R. B. Cell-Penetrating Peptides and Antimicrobial
739 Peptides: How Different Are They? *Biochem. J.* **2006**, *399* (1), 1–7.
- 740 (55) Nepal, D.; Geckeler, K. E. Proteins and Carbon Nanotubes: Close Encounter in Water. *Small*
741 **2007**, *3* (7), 1259–1265.
- 742 (56) Jacobson, K. H.; Gunsolus, I. L.; Kuech, T. R.; Troiano, J. M.; Melby, E. S.; Lohse, S. E.; Hu, D.;
743 Chrisler, W. B.; Murphy, C. J.; Orr, G.; et al. Lipopolysaccharide Density and Structure Govern
744 the Extent and Distance of Nanoparticle Interaction with Actual and Model Bacterial Outer
745 Membranes. *Environ. Sci. Technol.* **2015**, *49* (17), 10642–10650.
- 746 (57) Shang, L.; Nienhaus, K.; Jiang, X.; Yang, L.; Landfester, K.; Mailänder, V.; Simmet, T.;
747 Nienhaus, G. U. Nanoparticle Interactions with Live Cells: Quantitative Fluorescence Microscopy
748 of Nanoparticle Size Effects. *Beilstein J. Nanotechnol.* **2014**, *5* (1), 2388–2397.
- 749 (58) Schuergers, N.; Wilde, A. Appendages of the Cyanobacterial Cell. *Life* **2015**, *5* (1), 700–715.
- 750 (59) Dienst, D.; Dühring, U.; Mollenkopf, H. J.; Vogel, J.; Golecki, J.; Hess, W. R.; Wilde, A. The
751 Cyanobacterial Homologue of the RNA Chaperone Hfq Is Essential for Motility of *Synechocystis*
752 Sp. PCC 6803. *Microbiology* **2008**, *154* (10), 3134–3143.
- 753 (60) Duggan, P. S.; Gottardello, P.; Adams, D. G. Molecular Analysis of Genes in *Nostoc Punctiforme*
754 Involved in Pilus Biogenesis and Plant Infection. *J. Bacteriol.* **2007**, *189* (12), 4547–4551.
- 755 (61) Gao, Y.; Li, M.; Chen, B.; Shen, Z.; Guo, P.; Wientjes, M. G.; Au, J. L.-S. Predictive Models of
756 Diffusive Nanoparticle Transport in 3-Dimensional Tumor Cell Spheroids. *AAPS J.* **2013**, *15* (3),
757 816–831.
- 758 (62) Giraldo, J. P.; Wu, H.; Newkirk, G. M.; Kruss, S. Nanobiotechnology Approaches for Engineering
759 Smart Plants. *Nat. Nanotechnol.* **2019**, *14*, 541–553.
- 760 (63) Schuergers, N.; Lenn, T.; Kampmann, R.; Meissner, M. V.; Esteves, T.; Temerinac-Ott, M.;
761 Korvink, J. G.; Lowe, A. R.; Mullineaux, C. W.; Wilde, A. Cyanobacteria Use Micro-Optics to
762 Sense Light Direction. *Elife* **2016**, *5*, 1–16.

- 763 (64) Zheng, M.; Jagota, A.; Semke, E. D.; Diner, B. A.; Mclean, R. S.; Lustig, S. R.; Richardson, R. E.;
764 Tassi, N. G. DNA-Assisted Dispersion and Separation of Carbon Nanotubes. *Nat. Mater.* **2003**, 2
765 (5), 338–342.
- 766 (65) Reuel, N. F.; Ahn, J.; Kim, J.; Zhang, J.; Boghossian, A. A.; Mahal, L. K.; Strano, M. S.
767 Transduction of Glycan-Lectin Binding Using Near-Infrared Fluorescent Single-Walled Carbon
768 Nanotubes for Glycan Profiling. *J. Am. Chem. Soc.* **2011**, 133, 17923–17933.
- 769 (66) Rippka, R.; Deruelles, J.; Waterbury, J. B.; Herdman, M.; Stanier, R. Y. Generic Assignments,
770 Strain Histories and Properties of Pure Cultures of Cyanobacteria. *J. Gen. Microbiol.* **1979**, 111
771 (1), 1–61.
- 772 (67) Schuergers, N.; Nürnberg, D. J.; Wallner, T.; Mullineaux, C. W.; Wilde, A. PilB Localization
773 Correlates with the Direction of Twitching Motility in the Cyanobacterium *Synechocystis* Sp. PCC
774 6803. *Microbiology* **2015**, 161 (2015), 960–966.
- 775 (68) Gao, Z.; Oudjedi, L.; Faes, R.; Moroté, F.; Jaillet, C.; Poulin, P.; Lounis, B.; Cognet, L. Optical
776 Detection of Individual Ultra-Short Carbon Nanotubes Enables Their Length Characterization
777 down to 10 Nm. *Sci. Rep.* **2015**, 5, 1–10.
- 778 (69) Jin, H.; Heller, D. a.; Sharma, R.; Strano, M. S. Size-Dependent Cellular Uptake and Expulsion of
779 Single-Walled Carbon Nanotubes: Single Particle Tracking and a Generic Uptake Model for
780 Nanoparticles. *ACS Nano* **2009**, 3 (1), 149–158.
- 781 (70) Ritchie, R. J. Consistent Sets of Spectrophotometric Chlorophyll Equations for Acetone, Methanol
782 and Ethanol Solvents. *Photosynth. Res.* **2006**, 89 (1), 27–41.
- 783 (71) Currie, J.; Wilson, D. I. OPTI, Lowering the Barrier Between Open Source Optimizers and the
784 Industrial MATLAB User. *Found. Comput. Process Oper.* **2012**.

785